Joint wave-equation inversion of time-lapse seismic data

Gboyega Ayeni and Biondo Biondi

ABSTRACT

We discuss two regularized least-squares inversion formulations for time-lapse seismic imaging. Differences in acquisition geometries of baseline and monitor datasets or the presence of a complex overburden can degrade the quality of the time-lapse seismic signature. In such a scenario, the time-lapse amplitude information are poor indicators of the true reservoir property changes. Although the migration operator accurately images the seismic data, it does not remove these amplitude distortions. We pose time-lapse imaging as joint linear inverse problems that utilize concatenations of a target-oriented approximation to the least squares imaging Hessian. In one of the two formulations considered, outputs are inverted time-lapse images, while in the other, outputs are evolving images of the study area. Using a 2D-synthetic sub-salt model, we demonstrate that either joint-inversion formulation can attenuate overburden and geometry artifacts in time-lapse images and that joint wave-equation inversion yields more accurate results than migration or separate inversion.

INTRODUCTION

Hydrocarbon exploration and production has gradually shifted from simple to complex geological environments. Relatively simple imaging and monitoring objectives (e.g. anticlinal-type traps) have been replaced by more complex ones (e.g., sub-salt reservoirs and stratigraphic traps). Since most of the current time-lapse seismic imaging technologies are inadequate in many emerging frontiers, new imaging and monitoring methods are required. In addition, differences almost always exist between acquisition geometries of different seismic datasets. Such geometry differences may be due to new (or more efficient) acquisition systems and design, production facilities (absent at the time of the baseline survey) or nature (e.g., ocean currents).

Our goal is to attenuate artifacts from two major sources:

1. poor and uneven sub-surface illumination in reservoirs under complex overburden, and
2. disparities in acquisition geometries of the baseline and monitor surveys.

We achieve these objectives by simultaneously inverting migrated images from different vintages with a target-oriented approximation (Valenciano, 2008) to the linear least-squares wave-equation Hessian. The Hessian operator in this problem can be regarded as a set of non-stationary deconvolution filters in a single survey, or a concatenation of sub-matrices built from such filters in multiple surveys. We discuss two joint-inversion formulations of the seismic monitoring problem:

1. regularized joint-inversion for image differences (RJID):
    - input: staggered sums of migrated images, and
    - output: inverted baseline image and image differences between successive surveys;
2. regularized joint-inversion of multiple images (RJMI)
    - input: migrated images for all surveys,
    - output: inverted images for all input surveys.

Solving a single joint-inversion problem enables the incorporation of prior knowledge of the reservoir location, extent and geometry, temporal constraints or information from other sources (e.g., production history-matching).

As previously noted, inputs into the RJID formulation are staggered sums of migrated images from multiple surveys and the outputs are inverted baseline and time-lapse images between successive surveys. Since the imaging and monitoring objectives are decoupled, different regularization schemes can be defined for the baseline and time-lapse images. Inputs and outputs to RJMI are migrated images and corresponding inverted images respectively. RJMI differs from separate inversion, because a coupling operator introduces desirable temporal constraints during inversion.

In order to arrive at both formulations, we have assumed that the background baseline velocity model is known and that it changes slowly between surveys. We also assume that such small velocity changes have negligible impact on wave propagation through the earth, at least to the top of the reservoir. Where there are noticeable displacements between images — as a result of significant velocity changes or geomechanical effects around the reservoir — an event alignment step (Hale, 2007) can be applied prior to inversion.

In this paper, we briefly summarize the seismic monitoring problem, and then we discuss the basic theory of linear least-squares inversion and its extension to the RJID and RJMI formulations for an arbitarary number of surveys. Finally, using six datasets from a 2D-synthetic sub-salt model, we show that both joint-inversion formulations yield noticeably improved results over migration or separate inversion.

BACKGROUND

There is a wide range of published work on the most important considerations for time-lapse seismic monitoring. For example, Batzle and Wang (1992) outline important rock and fluid relationships; Lumley (1995), Rickett and Lumley (2001), Calvert (2005), and Johnston (2005) discuss important processing and practical applications; and Lefeuvre et al. (2003), Whitcombe et al. (2004), and Zou et al. (2006) showed successful case studies. Ayeni and Biondi (2008) discuss additional considerations and previous work related to seismic monitoring of hydrocarbon reservoirs.

Nemeth et al. (1999), Kuhl and Sacchi (2001), Clapp (2005), and Valenciano (2008) have shown that linear least-squares wave-equation migration of seismic data improves structural and amplitude information. We demonstrate that an extension of least-squares migration to the time-lapse imaging can improve time-lapse amplitude information, especially if all available data are jointly inverted. Previous authors have discussed joint-inversion applications, including impedance inversion (Sarkar et al., 2003), ray-tomography (Ajo-Franklin et al., 2005) and wave-equation velocity analysis (Albertin et al., 2006). Lumley et al. (2003) show that improvements can be made to time-lapse processing through *simultaneous processing*. Dynamic imaging strategies that utilize aspects of spatio-temporal regularization have also been discussed in other scientific disciplines (Schmitt and Louis, 2002; Schmitt et al., 2002; Zhang et al., 2005; Kindermann and Leitao, 2007).

A joint wave-equation inversion formulation of the time-lapse imaging problem has the advantage that the attenuation of image differences is based on the physics of wave propagation, making it less susceptible to removal of true time-lapse changes than conventional methods. The method proposed by Ajo-Franklin et al. (2005) for tomographic inversion can be directly extended to wave-equation inversion, and it actually forms a first step in the RJMI formulation. Such direct extension to wave-equation migration is too expensive, requiring at least one set of migration and modeling per survey per iteration. In most practical inversion problems, parameter selection requires that the inversion procedure be carried out more than once. By precomputing the Hessian operators, we are able to test different regularization schemes and parameters for the inversion at several orders of magnitude cheaper than directly solving the least-squares migration problem. In addition, we avoid the use of matching filters which can have unpredictable effects on time-lapse changes within the reservoir (Lumley et al., 2003).

THEORY

Linear inversion

Given a linear modeling operator $\mathbf{L}$, the seismic data $\mathbf{d}$ can be computed as

$$\mathbf{Lm} = \mathbf{d}, \tag{1}$$

where $\mathbf{m}$ is the reflectivity model. The modeling operator, $\mathbf{L}$, in this study, represents the seismic acquisition process. Two different surveys — say a baseline and monitor — acquired at different times ($\mathbf{t = 0}$ and $\mathbf{t = 1}$ respectively) over the same earth model can be represented as follows:

$$\begin{aligned} \mathbf{L}_0\mathbf{m}_0 &= \mathbf{d}_0, \\ \mathbf{L}_1\mathbf{m}_1 &= \mathbf{d}_1, \end{aligned} \tag{2}$$

where $\mathbf{m}_0$ and $\mathbf{m}_1$ are respectively the reflectivity models at the times when the datasets $\mathbf{d}_0$ and $\mathbf{d}_1$ were acquired, and $\mathbf{L}_0$ and $\mathbf{L}_1$ are the modeling operators defining the acquisition process for the two surveys (baseline and monitor).

The quadratic cost functions for equation 2 are given by

$$\begin{aligned} S(\mathbf{m_0}) &= \|\mathbf{L}_0\mathbf{m}_0 - \mathbf{d}_0\|^2, \\ S(\mathbf{m_1}) &= \|\mathbf{L}_1\mathbf{m}_1 - \mathbf{d}_1\|^2, \end{aligned} \tag{3}$$

and the least-squares solutions are

$$\begin{aligned} \hat{\mathbf{m}}_0 &= (\mathbf{L'}_0\mathbf{L}_0)^{-1}\mathbf{L'}_0\mathbf{d}_0 = (\mathbf{L'}_0\mathbf{L}_0)^{-1}\tilde{\mathbf{m}}_0 = \mathbf{H}_0^{-1}\tilde{\mathbf{m}}_0, \\ \hat{\mathbf{m}}_1 &= (\mathbf{L'}_1\mathbf{L}_1)^{-1}\mathbf{L'}_1\mathbf{d}_1 = (\mathbf{L'}_1\mathbf{L}_1)^{-1}\tilde{\mathbf{m}}_1 = \mathbf{H}_1^{-1}\tilde{\mathbf{m}}_1, \end{aligned} \tag{4}$$

where $\tilde{\mathbf{m}}_0$ and $\tilde{\mathbf{m}}_1$ are the migrated baseline and monitor images, $\hat{\mathbf{m}}_0$ and $\hat{\mathbf{m}}_1$ are the inverted images, $\mathbf{L'}_0$ and $\mathbf{L'}_1$ are the migration operators (adjoints to the modeling operators $\mathbf{L}_0$ and $\mathbf{L}_1$ respectively), and $\mathbf{H}_0 \equiv \mathbf{L'}_0\mathbf{L}_0$ and $\mathbf{H}_1 \equiv \mathbf{L'}_1\mathbf{L}_1$, are the Hessian matrices. Here, and in other parts of this paper, the symbol $'$ denotes transposed complex conjugate. These formulations are based on (but not limited to) one-way wave-equation extrapolation methods.

The Hessian matrices are the second derivatives of the cost functions (equation 3) with respect to all model points in the image. Because the Hessian matrices are generally not invertible for almost any practical scenario, equation 4 is solved iteratively as follows:

$$\begin{aligned} \mathbf{H}_0\hat{\mathbf{m}}_0 &= \tilde{\mathbf{m}}_0, \\ \mathbf{H}_1\hat{\mathbf{m}}_1 &= \tilde{\mathbf{m}}_1. \end{aligned} \tag{5}$$

An inverted time-lapse image, $\Delta\hat{\mathbf{m}}$, can be obtained as the difference between the two images, $\hat{\mathbf{m}}_1$ and $\hat{\mathbf{m}}_0$, obtained from equation 5:

$$\Delta\hat{\mathbf{m}} = \hat{\mathbf{m}}_1 - \hat{\mathbf{m}}_0. \tag{6}$$

We will refer to the method of computing the time-lapse image using equation 6 as *separate inversion* throughout the rest of this paper.

Joint-inversion

Two joint-inversion formulations are discussed in the following sections.

Joint-inversion for image differences (JID)

First, we re-formulate the data modeling operations for the two surveys in equation 2 as follows:

$$\begin{aligned} \mathbf{L}_0\mathbf{m}_0 &= \mathbf{d}_0, \\ \mathbf{L}_1(\mathbf{m}_0 + \Delta\mathbf{m}) &= \mathbf{d}_1, \end{aligned} \tag{7}$$

where $\mathbf{m}_0 + \Delta\mathbf{m} = \mathbf{m}_1$. In matrix form, these expressions can be combined to give

$$\begin{bmatrix} \mathbf{L}_0 & \mathbf{0} \\ \mathbf{L}_1 & \mathbf{L}_1 \end{bmatrix} \begin{bmatrix} \mathbf{m}_0 \\ \Delta\mathbf{m} \end{bmatrix} = \begin{bmatrix} \mathbf{d}_0 \\ \mathbf{d}_1 \end{bmatrix}. \tag{8}$$

In principle, using an iterative solver, a least-squares solution to equation 8 can be obtained by minimizing the cost function

$$S(\mathbf{m_0}, \Delta\mathbf{m}) = \left|\left| \begin{bmatrix} \mathbf{L}_0 & \mathbf{0} \\ \mathbf{L}_1 & \mathbf{L}_1 \end{bmatrix} \begin{bmatrix} \mathbf{m}_0 \\ \Delta\mathbf{m} \end{bmatrix} - \begin{bmatrix} \mathbf{d}_0 \\ \mathbf{d}_1 \end{bmatrix} \right|\right|^2. \tag{9}$$

The computational cost of this approach is proportional to the number of iterations times at least twice the cost of one set of migrations — since each iteration requires at least one modeling and one migration for the baseline and monitor datasets. Since several iterations would typically be required to reach convergence, and the inversion process would usually be repeated several times to fine-tune inversion parameters, the overall cost of this scheme will be high. An important advantage of the JID (or JMI) formulation is that modifications can be made to inversion parameters and the inversion repeated several times without the need for new migration or modeling. The least-squares solution to equation 8 is given by

$$\begin{bmatrix} \mathbf{L'}_0\mathbf{L}_0 + \mathbf{L'}_1\mathbf{L}_1 & \mathbf{L'}_1\mathbf{L}_1 \\ \mathbf{L'}_1\mathbf{L}_1 & \mathbf{L'}_1\mathbf{L}_1 \end{bmatrix} \begin{bmatrix} \hat{\mathbf{m}}_0 \\ \Delta\hat{\mathbf{m}} \end{bmatrix} = \begin{bmatrix} \mathbf{L'}_0 & \mathbf{L'}_1 \\ \mathbf{0} & \mathbf{L'}_1 \end{bmatrix} \begin{bmatrix} \mathbf{d}_0 \\ \mathbf{d}_1 \end{bmatrix} = \begin{bmatrix} \tilde{\mathbf{m}}_0 + \tilde{\mathbf{m}}_1 \\ \tilde{\mathbf{m}}_1 \end{bmatrix}, \tag{10}$$

or

$$\begin{bmatrix} \mathbf{H}_0 + \mathbf{H}_1 & \mathbf{H}_1 \\ \mathbf{H}_1 & \mathbf{H}_1 \end{bmatrix} \begin{bmatrix} \hat{\mathbf{m}}_0 \\ \Delta\hat{\mathbf{m}} \end{bmatrix} = \begin{bmatrix} \tilde{\mathbf{m}}_0 + \tilde{\mathbf{m}}_1 \\ \tilde{\mathbf{m}}_1 \end{bmatrix}, \tag{11}$$

which can be recast as

$$\begin{bmatrix} \hat{\mathbf{m}}_0 \\ \Delta\hat{\mathbf{m}} \end{bmatrix} = \begin{bmatrix} \mathbf{H}_0 + \mathbf{H}_1 & \mathbf{H}_1 \\ \mathbf{H}_1 & \mathbf{H}_1 \end{bmatrix}^{-1} \begin{bmatrix} \tilde{\mathbf{m}}_0 + \tilde{\mathbf{m}}_1 \\ \tilde{\mathbf{m}}_1 \end{bmatrix}. \tag{12}$$

Thus, the inverted baseline and time-lapse images ($\hat{\mathbf{m}}_0$ and $\Delta\hat{\mathbf{m}}$ respectively) can be obtained from equation 12. However, since the Hessian matrices $\mathbf{H}_0$ and $\mathbf{H}_1$ (and hence the joint Hessian operator) are not invertible, equation 11 is solved iteratively. We have extended equation 11 to multiple surveys (Appendix A). When multiple surveys are available, the outputs of the JID formulation are the inverted baseline image and image differences between successive surveys.

Joint-inversion of multiple images (JMI)

The data modeling operations for two surveys can be written as follows

$$\begin{bmatrix} \mathbf{L}_0 & \mathbf{0} \\ \mathbf{0} & \mathbf{L}_1 \end{bmatrix} \begin{bmatrix} \mathbf{m}_0 \\ \mathbf{m}_1 \end{bmatrix} = \begin{bmatrix} \mathbf{d}_0 \\ \mathbf{d}_1 \end{bmatrix}. \tag{13}$$

In principle, it is possible to solve for a least-squares solution to equation 13 by minimizing the cost function

$$S(\mathbf{m_0}, \mathbf{m_1}) = \left|\left| \begin{bmatrix} \mathbf{L}_0 & \mathbf{0} \\ \mathbf{0} & \mathbf{L}_1 \end{bmatrix} \begin{bmatrix} \mathbf{m}_0 \\ \mathbf{m}_1 \end{bmatrix} - \begin{bmatrix} \mathbf{d}_0 \\ \mathbf{d}_1 \end{bmatrix} \right|\right|^2. \tag{14}$$

As discussed in the JID formulation, this would be too expensive to be practical since the cost of one iteration is at least the cost of four migrations. Ajo-Franklin et al. (2005) have shown a tomographic example of this formulation, but since each migration is orders of magnitudes more expensive than ray-based tomography, this approach would be too expensive for wave-equation inversion. Therefore, we reformulate equation 14 as

$$\begin{bmatrix} \mathbf{L'}_0\mathbf{L}_0 & \mathbf{0} \\ \mathbf{0} & \mathbf{L'}_1\mathbf{L}_1 \end{bmatrix} \begin{bmatrix} \hat{\mathbf{m}}_0 \\ \hat{\mathbf{m}}_1 \end{bmatrix} = \begin{bmatrix} \mathbf{L'}_0 & \mathbf{0}_1 \\ \mathbf{0} & \mathbf{L'}_1 \end{bmatrix} \begin{bmatrix} \mathbf{d}_0 \\ \mathbf{d}_1 \end{bmatrix} = \begin{bmatrix} \tilde{\mathbf{m}}_0 \\ \tilde{\mathbf{m}}_1 \end{bmatrix}, \tag{15}$$

or

$$\begin{bmatrix} \mathbf{H}_0 & \mathbf{0} \\ \mathbf{0} & \mathbf{H}_1 \end{bmatrix} \begin{bmatrix} \hat{\mathbf{m}}_0 \\ \hat{\mathbf{m}}_1 \end{bmatrix} = \begin{bmatrix} \tilde{\mathbf{m}}_0 \\ \tilde{\mathbf{m}}_1 \end{bmatrix}, \tag{16}$$

which can be written as

$$\begin{bmatrix} \hat{\mathbf{m}}_0 \\ \hat{\mathbf{m}}_1 \end{bmatrix} = \begin{bmatrix} \mathbf{H}_0 & \mathbf{0} \\ \mathbf{0} & \mathbf{H}_1 \end{bmatrix}^{-1} \begin{bmatrix} \tilde{\mathbf{m}}_0 \\ \tilde{\mathbf{m}}_1 \end{bmatrix}. \tag{17}$$

Thus, the inverted baseline and monitor images ($\hat{\mathbf{m}}_0$ and $\hat{\mathbf{m}}_1$ respectively) can be obtained from equation 17 and the time-lapse image as a difference between the two images as done in equation 5. Also, note that without coupling, as done in the next section, equation 16 is equivalent to equation 5. Since the Hessian matrices $\mathbf{H}_0$ and $\mathbf{H}_1$ (and hence the joint Hessian operator) are not invertible, equation 16 is solved iteratively. An extension of equation 16 to multiple surveys is given in Appendix A.

Joint-inversion with Regularization

In most seismic monitoring problems, the general geology and reservoir architecture of the study area are known — thus providing some information that can be used to determine appropriate regularization for the inversion. Such regularization incorporates prior knowledge of the reservoir geometry and location, and expectation of

changes in different parts of the study area. As shown in the Appendix, the regularized joint-inversion for image difference (RJID) for two surveys is given by

$$\left(\begin{bmatrix} \mathbf{H_0}+\mathbf{H_1} & \mathbf{H_1} \\ \mathbf{H_1} & \mathbf{H_1} \end{bmatrix} + \begin{bmatrix} \mathbf{R_{00}} & \mathbf{0} \\ \mathbf{0} & \mathbf{R_{11}} \end{bmatrix} + \begin{bmatrix} \mathbf{\Lambda_{00}} & \mathbf{0} \\ -\mathbf{\Lambda_{10}} & \mathbf{\Lambda_{11}} \end{bmatrix}\right) \begin{bmatrix} \hat{\mathbf{m}}_0 \\ \Delta\hat{\mathbf{m}}_1 \end{bmatrix} = \begin{bmatrix} \tilde{\mathbf{m}}_0+\tilde{\mathbf{m}}_1 \\ \tilde{\mathbf{m}}_1 \end{bmatrix}, \tag{18}$$

where

$$\begin{aligned} \mathbf{R_{ij}} &= \epsilon_\mathbf{i}\mathbf{R'}_\mathbf{i}\epsilon_\mathbf{j}\mathbf{R_j}, \\ \mathbf{\Lambda_{ij}} &= \zeta_\mathbf{i}\mathbf{\Lambda'}_\mathbf{i}\zeta_\mathbf{j}\mathbf{\Lambda_j}, \end{aligned} \tag{19}$$

while $\mathbf{R_0}$ and $\mathbf{R_1}$ are the spatial/imaging constraints for the baseline and time-lapse images respectively, and $\mathbf{\Lambda_0}$ and $\mathbf{\Lambda_1}$ the temporal regularization (or coupling) between the surveys. In the implementation of equation 19, the regularization terms, $\mathbf{R_{ij}}$ and $\mathbf{\Lambda_{ij}}$ are not explicitly computed, but instead, the appropriate operators $\mathbf{R_i}$ and $\mathbf{\Lambda_i}$ (and their adjoints, $\mathbf{R'_i}$ and $\mathbf{\Lambda'_i}$ respectively) are applied at each step of the inversion. The parameters $\epsilon_\mathbf{0}$ and $\epsilon_\mathbf{1}$ determine strength of the spatial regularization on the baseline and time-lapse images respectively, while $\zeta_\mathbf{0}$ and $\zeta_\mathbf{1}$ determine the coupling between surveys. The regularized joint-inversion of multiple images (RJMI) formulation for two surveys is given as

$$\left(\begin{bmatrix} \mathbf{H_0} & \mathbf{0} \\ \mathbf{0} & \mathbf{H_1} \end{bmatrix} + \begin{bmatrix} \mathbf{R_{00}} & \mathbf{0} \\ \mathbf{0} & \mathbf{R_{11}} \end{bmatrix} + \begin{bmatrix} \mathbf{\Lambda_{00}} & -\mathbf{\Lambda_{01}} \\ -\mathbf{\Lambda_{10}} & \mathbf{\Lambda_{11}} \end{bmatrix}\right) \begin{bmatrix} \hat{\mathbf{m}}_0 \\ \hat{\mathbf{m}}_1 \end{bmatrix} = \begin{bmatrix} \tilde{\mathbf{m}}_0 \\ \tilde{\mathbf{m}}_1 \end{bmatrix}. \tag{20}$$

The spatial regularization operator contains information on the structural geometry of the reservoir (or implied properties of correctly migrated gathers, e.g. horizontal angle gathers, or near-zero concentration of amplitudes in subsurface offset gathers), while the temporal regularization ensures that the reservoir changes evolve according to a reasonable scheme (e.g., smooth variation over time). The temporal regularization operator in the RJMI formulation is similar to that used in spatio-temporal tomographic inversion (Ajo-Franklin et al., 2005).

As shown in Appendix A, the general regularized joint-inversion problem can be written in compact notation as

$$[\mathbf{\Xi} + \Re + \mathbf{\Gamma}] \left[\hat{\mathbf{M}}\right] = \left[\tilde{\mathbf{M}}\right], \tag{21}$$

where $\mathbf{\Xi}$ is the Hessian operator, $\Re$ is the spatial/imaging regularization operator, $\mathbf{\Gamma}$ is the temporal regularization operator, $\hat{\mathbf{M}}$ is the model vector and $\tilde{\mathbf{M}}$ the data vector. Each of the components of the RJID and RJMI formulations are fully described in Appendix A.

Note that in the RJID formulation, the imaging (baseline inversion) and monitoring (time-lapse inversion) goals are decoupled, thus allowing for application of different regularization schemes. Since the baseline and time-lapse images are expected to have different desirable properties, the baseline ($\mathbf{R_0}$ and $\mathbf{\Lambda_0}$) and monitor ($\mathbf{R_1}$ to $\mathbf{R_N}$ and $\mathbf{\Lambda_0}$ to $\mathbf{\Lambda_N}$) regularization operators are different. The RJMI formulation is cheaper to solve, since the joint Hessian operator is less dense and with appropriate regularization, the results from the two formulations should be comparable.

Target-oriented Hessian

The computational cost of the full Hessian matrix for one survey (needless to say for multiple surveys) is prohibitive and not practical for any reasonably sized survey. Several authors have discussed possible approximations to the wave-equation Hessian (Shin et al., 2001; Rickett, 2003; Guitton, 2004; Valenciano, 2008; Symes, 2008; Tang, 2008b,a) . The wave-equation Hessian for synthetic seismic data, $\mathbf{d}\left(\mathbf{s},\mathbf{r};\omega\right)$ at a given frequency, ω, recorded by receiver $\mathbf{r}\left(x_r,y_r,z_r\right)$, from a shot $\mathbf{s}\left(x_s,y_s,z_s\right)$ and scattering point $\mathbf{x}(x,y,z)$, is given by

$$\mathbf{H}\left(\mathbf{x},\mathbf{y}\right)=\sum_{w}\omega^4\sum_{\mathbf{s}}\left|f'\left(s\right)\right|^2\mathbf{G}'\left(\mathbf{x},\mathbf{s};\omega\right)\mathbf{G}\left(\mathbf{y},\mathbf{s};\omega\right)\sum_{\mathbf{r}}\mathbf{G}'\left(\mathbf{x},\mathbf{r};\omega\right)\mathbf{G}\left(\mathbf{y},\mathbf{r};\omega\right), \quad (22)$$

where $\mathbf{y}(x,y,z)$ corresponds to all model points. A detailed derivation of the explicit wave-equation Hessian is given by Mulder and Plessix (2004).

Because reservoirs are typically limited in extent, the region of interest is usually smaller than the full image space. Thus, the required Hessian matrices are constructed for a region around the target zone and not for the full survey area. In this paper, we follow the target-oriented approach of Valenciano (2008) in the Hessian computation. Phase-encoding approximations to the target-oriented Hessian (Tang, 2008a) offer improved efficiency in the Hessian computation and are currently being explored as alternatives to the explicit method used in this paper.

The target oriented Hessian (Valenciano, 2008) is given by:

$$\begin{aligned}\mathbf{H}(\mathbf{x_T},\mathbf{x_T}+\mathbf{a_x}) = \quad & \textstyle\sum_w \omega^4 \quad \sum_{\mathbf{s}}\left|f'\left(s\right)\right|^2\mathbf{G}'(\mathbf{x_T},\mathbf{s};\omega)\mathbf{G}(\mathbf{x_T}+\mathbf{a_x},\mathbf{s};\omega) \\ & \sum_{\mathbf{r}}\mathbf{G}'(\mathbf{x_T},\mathbf{r};\omega)\mathbf{G}(\mathbf{x_T}+\mathbf{a_x},\mathbf{r};\omega),\end{aligned} \quad (23)$$

where $\mathbf{a_x}$ is the offset from the target image-point $\mathbf{x_T}$ defining the filter size and hence the number of off-diagonal terms to be computed. The filter size $\mathbf{a_x}$ can be determined heuristically or from an analysis of the amplitudes of filter coefficients away from the diagonal. As noted by Valenciano (2008), the frequency sampling required to prevent wrap-around artifacts for the local filter (or row of the Hessian) for a given image point is coarser than that used in migration. Examples of the target-oriented Hessian operator for the model in Figures 1 and three surveys are shown in Figures 2 and 3 for both RJID and RJMI.

In a single survey, each row of the Hessian is a point-spread function that describes the effects of the limited-bandwidth seismic waveform, geometry and illumination on a reflectivity spike in the subsurface. In multiple surveys, each band belonging to individual sub-matrices contains similar information from a single or combination of surveys as shown in equations A-25 and A-12. In addition, note that the empty bins in Figures 2 and 3 are neither computed nor stored and that because of the matrix symmetry, only one-half of its elements needs to be computed. The structure of the problem gives a large leeway for parallelization over several domains in both the Hessian computation and inversion. Finally, since we assume that there is not

Figure 1: Full impedance model. The box indicates the target area for which Figures 2 and 3 were computed, while the anomaly centered at distance 0m and depth 3000m represents the approximate location of reservoir change. The triangular block is a salt with velocity 4500m/s, while the surrounding sediments have velocities ranging from 2200m/s and 2700m/s. The densities range from 2.5g/cc to 3.0g/cc. [**ER**]

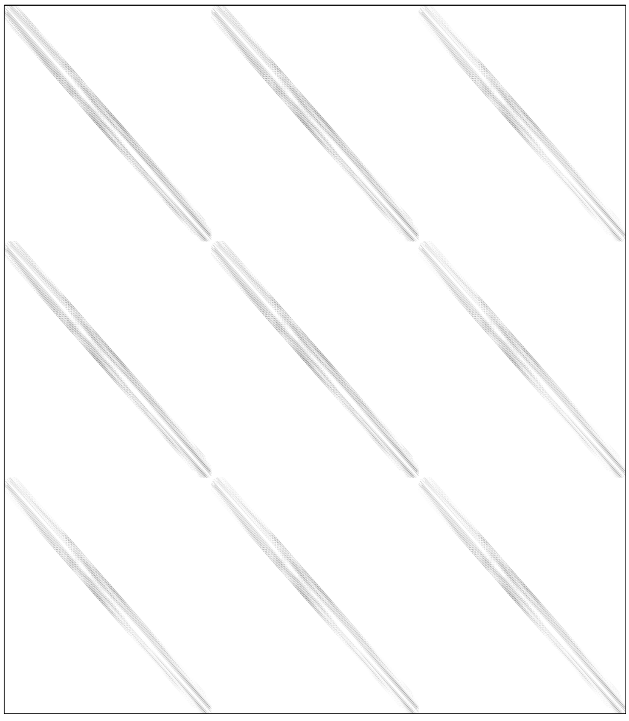

Figure 2: JID: Joint target-oriented Hessian operator for one baseline and two monitor surveys for the reservoir models in Figure 1. The dimension of the square matrix here and in Figure 3 is equal to the number of surveys times the size of the model space. This figure corresponds to the $\mathbf{\Xi}$ operator in equation A-24. Note however that the zeros (light regions in the matrices) were neither computed nor stored. [**NR**]

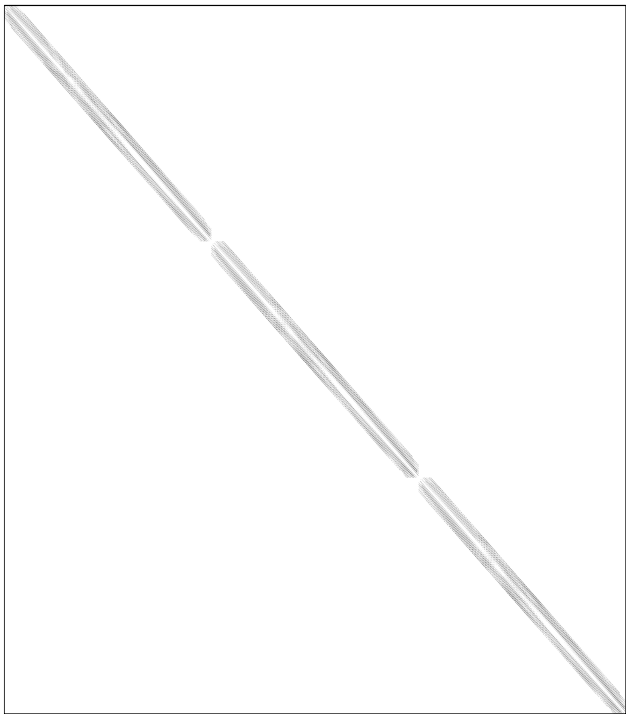

Figure 3: JMI: Joint target-oriented Hessian for one baseline and two monitor surveys for the reservoir models in Figure 1. See caption in Figure 2 for further description. [**NR**]

a significant variation in the background velocity between surveys, and since some shot and receiver locations would be re-occupied during the monitor survey(s), some Green's functions can be reused in the Hessian computation for different surveys.

NUMERICAL EXAMPLE

The inversion formulations were tested on synthetic datasets modeled for the 2D-synthetic sub-salt model in Figure 1. We simulated six datasets (representing different stages of production) using a variable-density acoustic finite-difference algorithm. Reservoir changes were modeled as an expanding Gaussian anomaly centered at x = 0m and z = 3000m. In order to simulate non-repeated acquisition geometries, we modeled all the datasets with spatially different geometries as summarized in Table 1. We modeled 76 shots spaced at 80m and 301 receivers spaced at 20m and for each survey, the receiver spread was kept constant while the shots move along. We consider that reflectivity change is most influenced by a change in the density within the reservoir and that there is not a significant change in the background velocity model between surveys. The spatial regularization operator is a gradient along reflector dips, while a temporal gradient was used to ensure temporal smoothness.

Figure 4 shows the migrated images for the six surveys, while corresponding illumination maps (diagonal of the Hessian) are shown in Figure 5. The irregular illumination patterns explain the uneven amplitudes of reflectors below the salt in Figure 4. Figure 6 shows the illumination-ratio (normalized rms-difference in illumination) between baseline and the monitor surveys, which measures of the variability

Table 1: Modeling parameters for synthetic datasets

	Shot/receiver depth	Shot/receiver spread
Geometry 1	0m	−3000 to 3000m
Geometry 2	100m	−3500 to 2500m
Geometry 3	200m	−2600 to 3400m
Geometry 4	40m	−2900 to 3100m
Geometry 5	240m	−3200 to 2800m
Geometry 6	300m	−2500 to 3500m

of illumination between surveys. We represent the variation in illumination at any image point as the illumination-ratio between the point-spread functions for the different surveys. For example, Figure 7 shows the point-spread functions at image point $[x = -200m, z = 2800m]$, while Figure 8 shows the coresponging illumination-ratio. The time-evolution of the true reflectivity model is shown in Figure 9 and the inversion goal is to reconstruct these. Figure 10 is the reflectivity change obtained from migration, while Figures 11 to 13 were obtained from separate inversion, RJID and RJMI respectively. Both the RJID and RJMI results contain less noise relative to migration (Figures 10) and separate inversion (Figures 11). No pre-processing was done to remove multiples from the data and hence these are expected to adversely affect the inversion.

DISCUSSION

Uneven illumination of the reservoir region as captured by the Hessian diagonal (Figure 5) and ratio (Figure 6) explain the high-amplitude artifacts observed in the migrated time-lapse images in Figure 10. The noticeable shadow zones in parts of the reservoir below the salt (Figure 4) result from the high impedance contrast at the salt-sediment boundary and the complex wave propagation. As shown by Ayeni and Biondi (2008), even where the survey geometries are perfectly repeated, uneven illumination below complex overburden can strongly distort time-lapse seismic amplitudes.

Since different geometries were used for all surveys in the numerical test, deterioration of the time-lapse amplitudes is due to a combined effect of geometry and complex overburden. The illumination-ratio maps (Figure 5) show the variability of illumination between surveys. Disparities in point-spread functions (Figure 8) suggest that the a diagonal approximation to the Hessian is insufficient to remove the unwanted artifacts. Although separately inverted time-lapse images in Figure 11 show some improvement in resolution over migration results (Figure 10), the images are dominated by the large amplitude residual artifacts. Time-lapse images obtained from joint-inversion using the RJID (Figure 12), and RJMI (Figure 13) formulations are less noisy than those from the migration (Figure 10) and separate inversion (Figure 11) and are comparable to the true reflectivity change in Figure 9. Since one-way

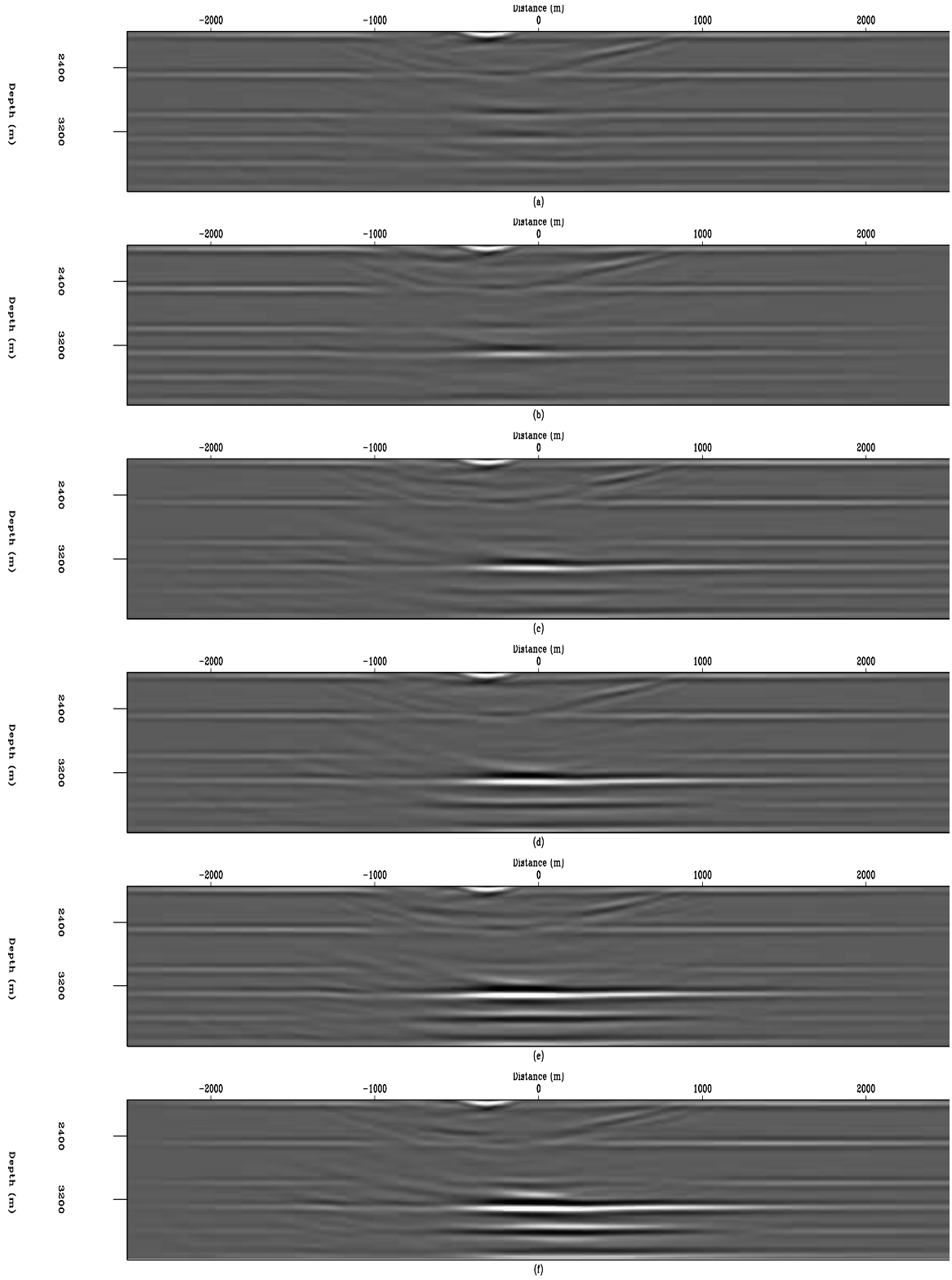

Figure 4: Migrated images obtained for six surveys (see modeling parameters in Table 1) for the target area in shown Figure 1. Figure (a) is the baseline image, while Figures (b)-(f) are images of the monitor images. Note the irregular amplitude patterns cause by the presence of the overlying salt structure.[**CR**]

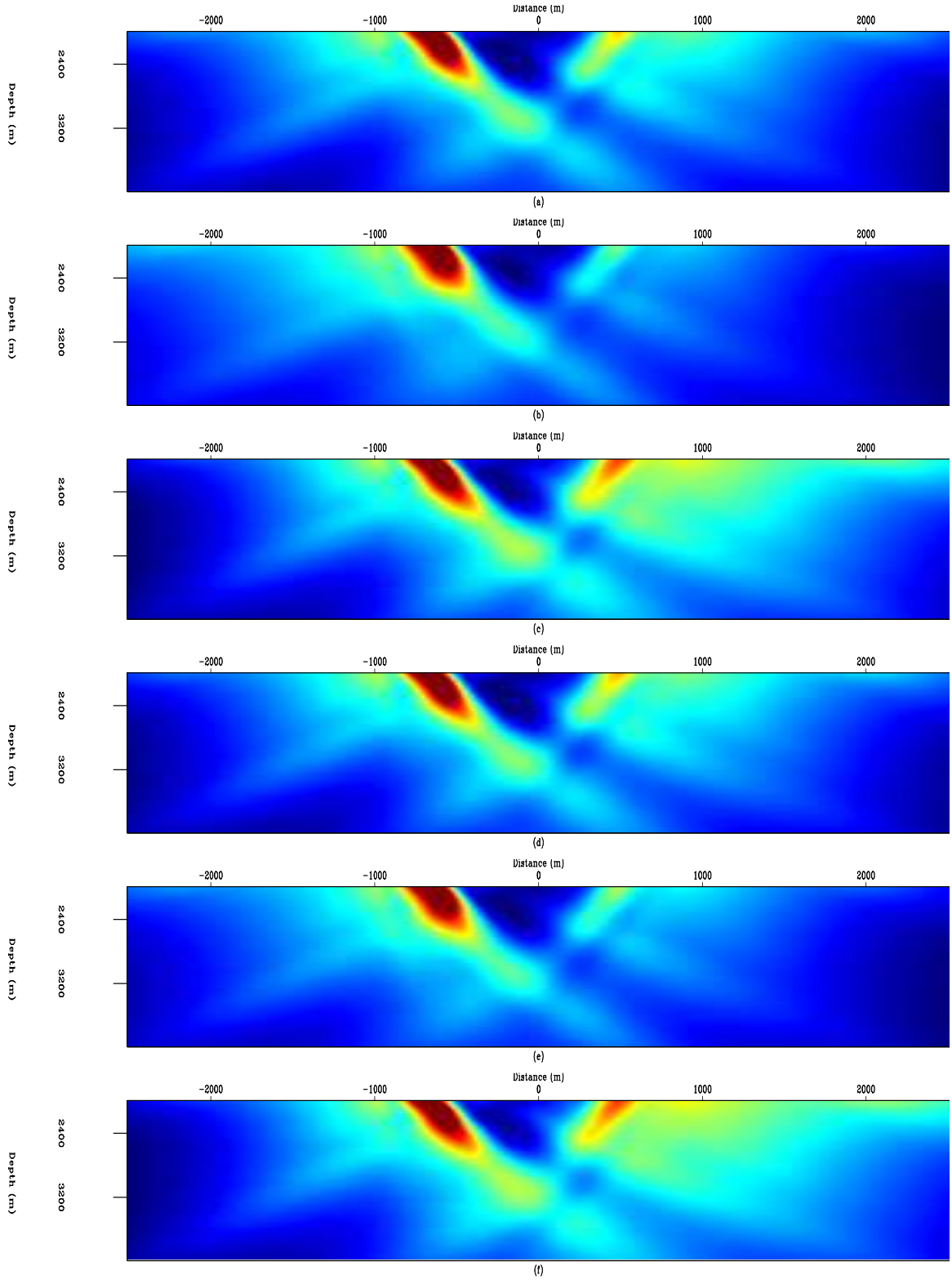

Figure 5: Illumination maps for the six surveys described in Table 1. Each section corresponds to the migrated sections in Figure 4 and explain the observed irregular seismic amplitudes. Light color represent high illumination and dark represents low illumination.[**CR**]

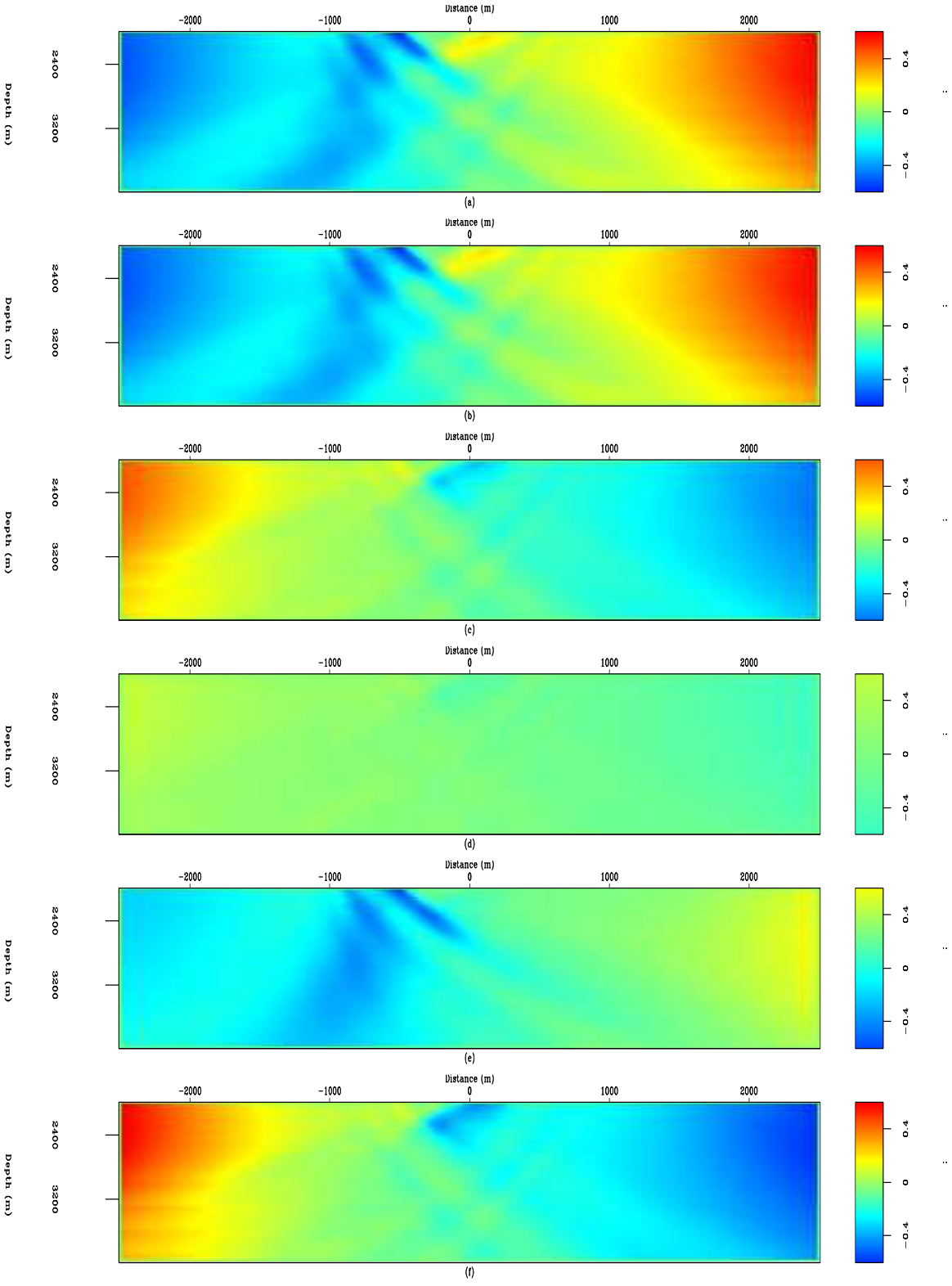

Figure 6: Base-Monitor illumination-ratio for the six surveys described in Table 1. Each section corresponds to a normalized rms-ratio (over 3x3 patches) between the Hessian diagonal of the monitor surveys (Figure 5b-f) to that of the baseline (Figure 5a).[**CR**]

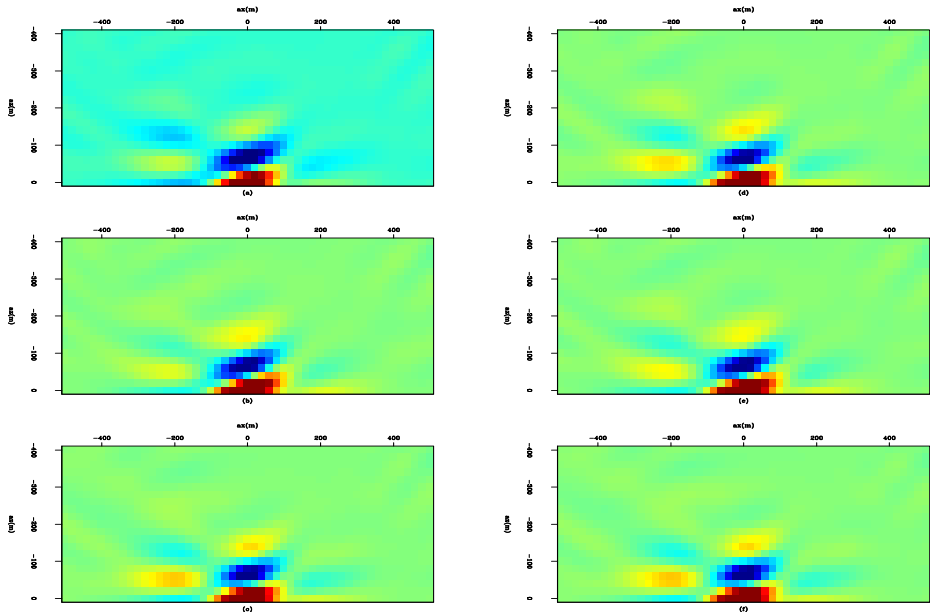

Figure 7: Point spread functions at the image point $[x = -200m, z = 2800m]$ for the six surveys in Figure 5. Each section corresponds to a row of the Hessian for the images in Figure 4a-f). Note that only one half of each filter is computed, since the Hessian matrix is symmetric.[**CR**]

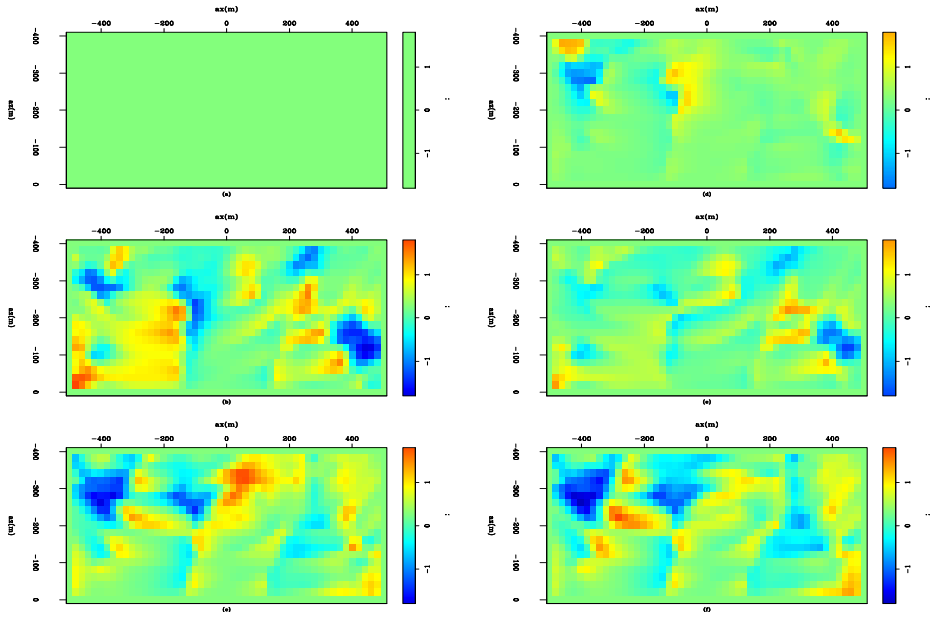

Figure 8: Base-Monitor illumination-ratio at image point $[x = -200m, z = 2800m]$ for the six surveys described in Table 1. section corresponds to a normalized rms-ratio (over 3x3 patches) between the point-spread functions (a row of the Hessian) of the monitor surveys (Figure 7b-f) to that of the baseline (Figure 7a).[**CR**]

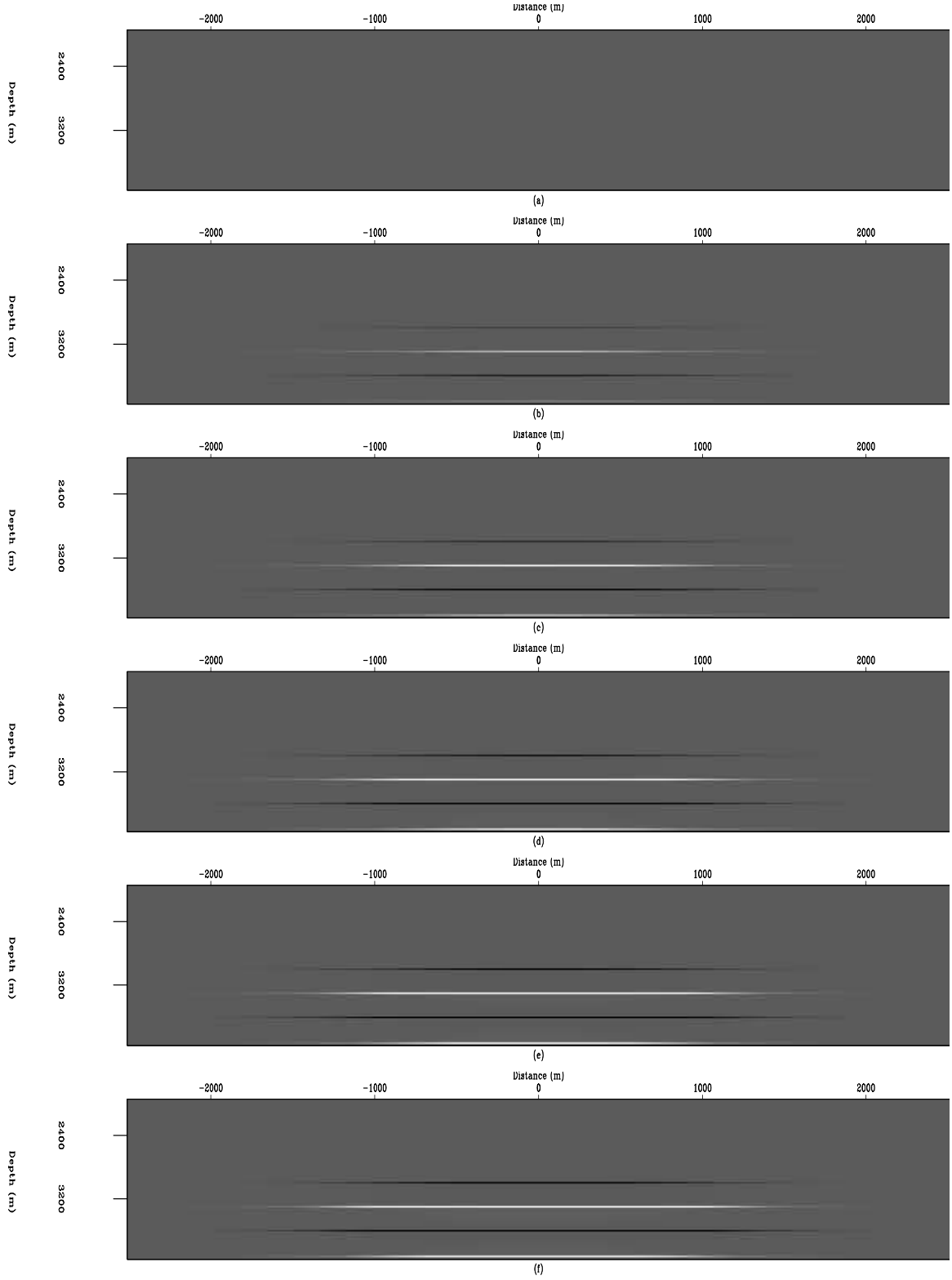

Figure 9: True cumulative time-lapse reflectivity images at the times for which the six surveys (Table 1) were modeled. These should be compared with the results in Figures 10 to 13.[**CR**]

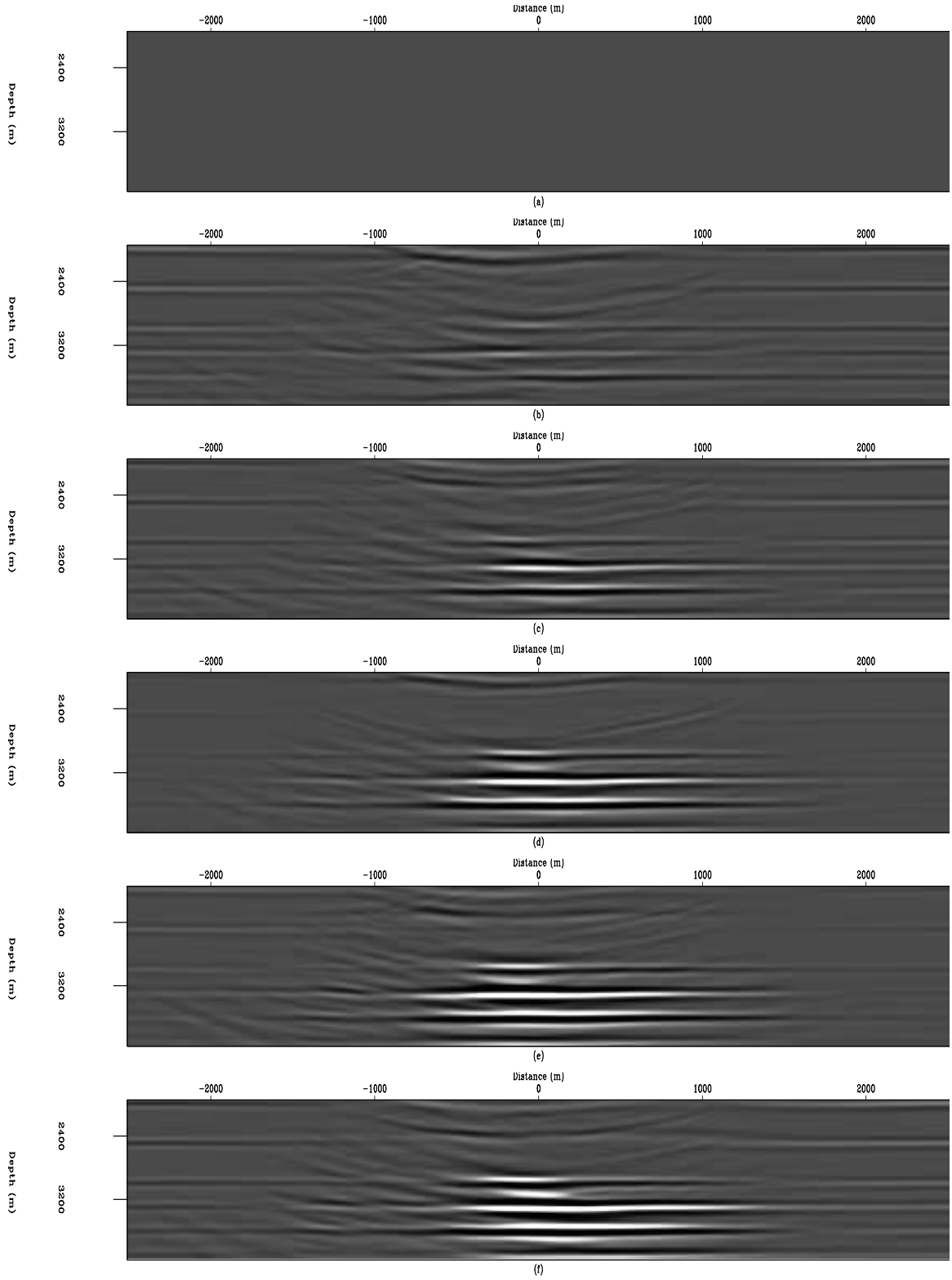

Figure 10: Migrated time-lapse at six different times corresponding to Figure 4. Each section shows the amplitude change between time 1 (baseline) and the time of the monitor survey. Note that the inversion has resulted in an increase in the noise amplitudes relative to migrated time-lapse images shown in Figure 10.[**CR**]

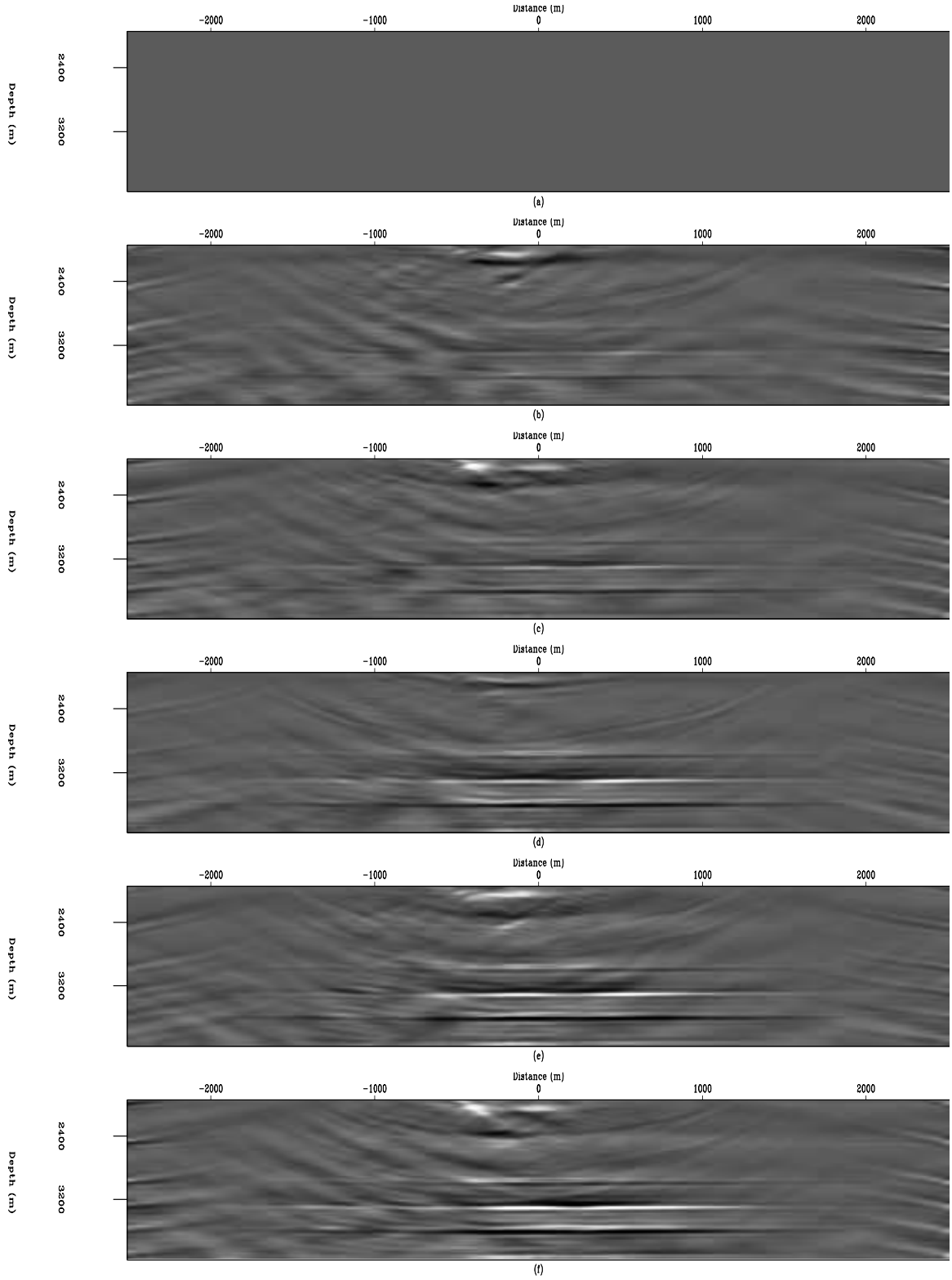

Figure 11: Separately inverted time-lapse images at six different times. Each section shows the amplitude change between time 1 (baseline) and the time of the monitor survey. Note that the inversion has resulted in an increase in the noise amplitudes relative to migrated time-lapse images shown in Figure 10.[**CR**]

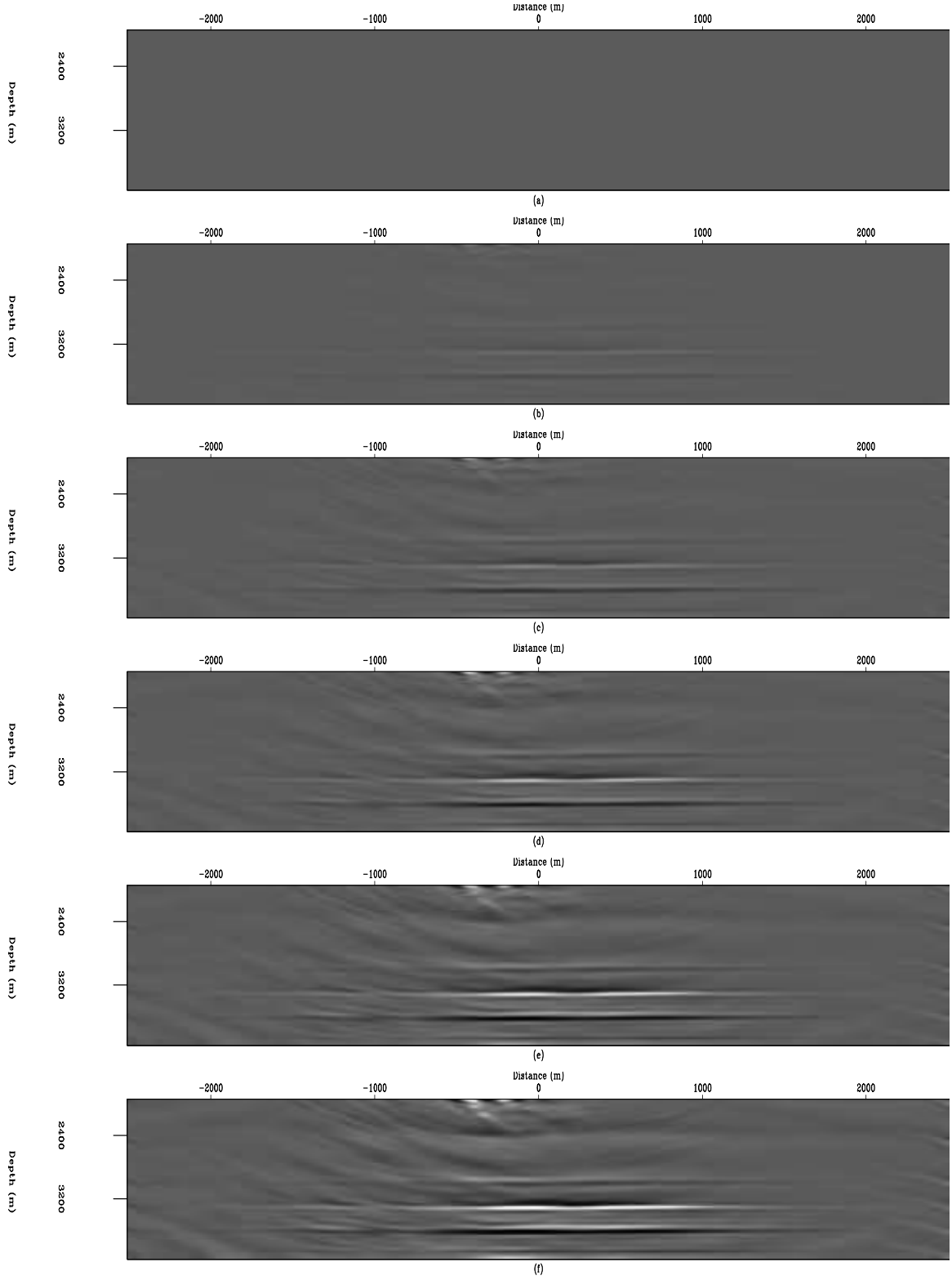

Figure 12: RJID: Jointly inverted time-lapse images at six different times. Each section shows the amplitude change between time 1 (baseline) and the time of the monitor survey. Compare these results to Figures 9, 10, 11 and 13.[**CR**]

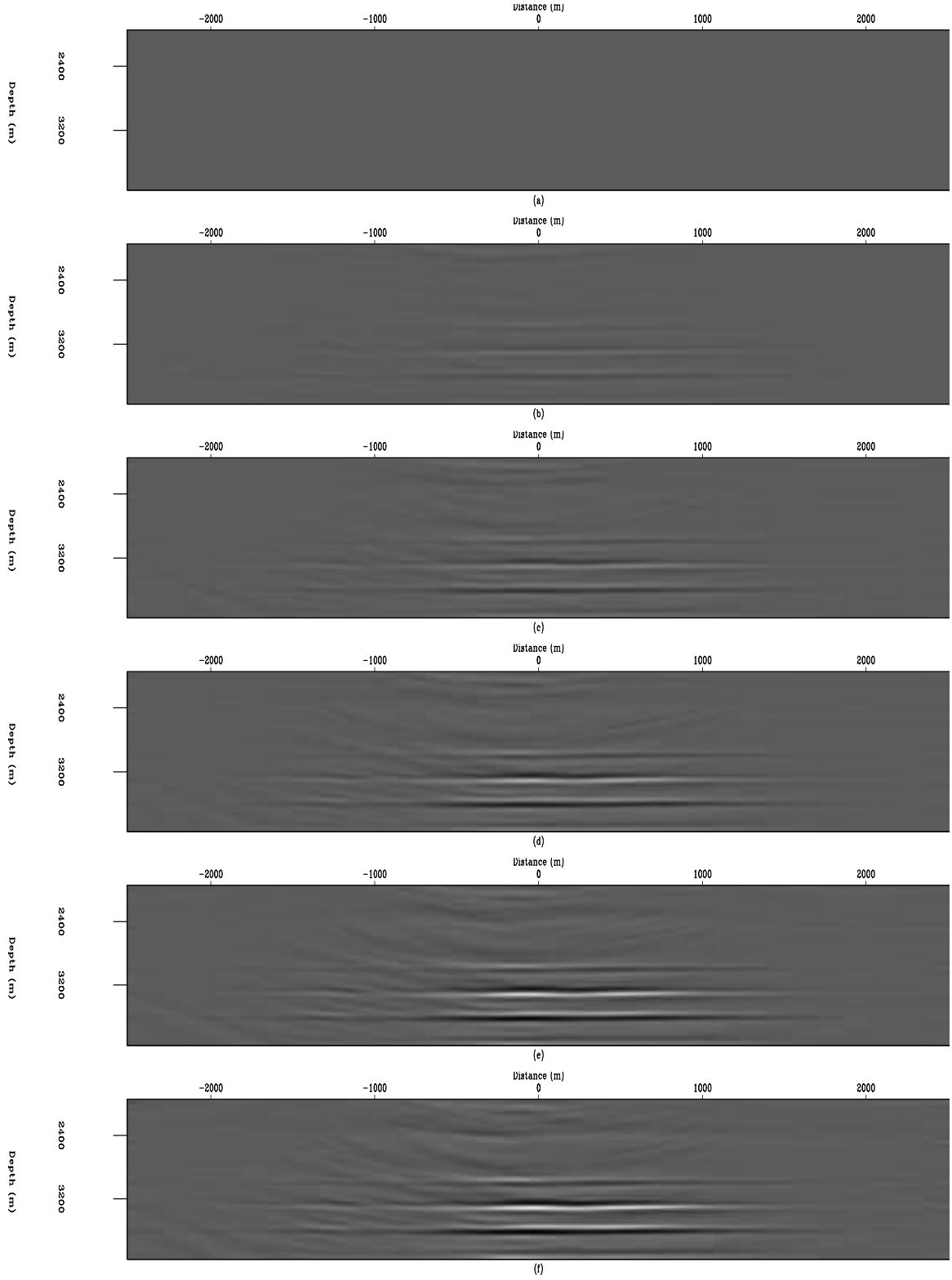

Figure 13: RJMI: Jointly inverted time-lapse images at six different times. Each section shows the amplitude change between time 1 (baseline) and the time of the monitor survey. Compare these results to Figures 9, 10, 11 and 12.[**CR**]

operators were used in this study, the Hessian contains no information regarding secondary events such as multiples. Residual effects of internal multiples due to the salt persist in the inversion results but are significantly suppressed in the jointly inverted images. In many cases of interest, multiple energy will be sufficiently attenuated or may not fall within the target region, and thus have little impact on the inversion.

CONCLUSIONS

We have proposed two regularized least-squares inversion formulations for time-lapse seismic imaging. -hese formulations arise from the linearized least-square wave-equation inversion. By using a target-oriented approximation to the least-squares Hessian with appropriate spatial and temporal regularization, we have shown that image difference due to geometry dissimilarity and complex overburden can be attenuated. We show that we can directly invert for image differences (RJID) or multiple images (RJMI) using a concatenation of target-oriented Hessian operators and combinations of migrated images. From numerical tests using a synthetic 2D-subsalt model, we conclude that both the RJID and RJMI joint-inversion formulations give more accurate time-lapse images than either migration or separate inversion.

REFERENCES

Ajo-Franklin, J. B., J. Urban, and J. M. Harris, 2005, Temporal integration of seismic traveltime tomography: SEG Technical Program Expanded Abstracts, **24**, 2468–2471.

Albertin, U., P. Sava, J. Etgen, and M. Maharramov, 2006, Adjoint wave-equation velocity analysis: SEG Technical Program Expanded Abstracts, **25**, 3345–3349.

Ayeni, G. and B. Biondi, 2008, Time-lapse inversion: SEP 134.

Batzle, M. and Z. Wang, 1992, Seismic properties of pore fluids: Geophysics, **57**, 1396–1408.

Calvert, R., 2005, Insights and methods for 4D reservoir monitoring and characterization: SEG/EAGE DISC (Distinguished Instructor Lecture Course).

Clapp, M. L., 2005, Imaging under salt: illumination compensation by regularized inversion: PhD thesis, Stanford University.

Guitton, A., 2004, Amplitude and kinematic corrections of migrated images for nonunitary imaging operators: Geophysics, **69**, 1017–1024.

Hale, D., 2007, A method for estimating apparent displacement vectors from time-lapse seismic images: CWP Report-566.

Johnston, D., 2005, Time-lapse 4D technology: Reservoir surveillance: AAPG Search and Discovery.

Kindermann, S. and A. Leitao, 2007, Regularization by dynamic programming: Journal of Inverse and Ill-posed Problems, **15**, 295–310.

Kuhl, H. and M. Sacchi, 2001, Generalized least-squares dsr migration using a com-

mon angle imaging condtion: 71st Annual International Meeting, Expanded Abstracts, 1025–1028, SEG.

Lefeuvre, F., Y. Kerdraon, J. Peliganga, S. Medina, P. Charrier, R. L'Houtellier, and D. Dubucq, 2003, Improved reservoir understanding through rapid and effective 4D: Girassol field, Angola, West Africa: SEG Technical Program Expanded Abstracts, **22**, 1334–1337.

Lumley, D., D. C. Adams, M. Meadows, S. Cole, and R. Wright, 2003, 4d seismic data processing issues and examples: SEG Technical Program Expanded Abstracts, **22**, 1394–1397.

Lumley, D. E., 1995, Seismic time-lapse monitoring of subsurface fluid flow: PhD thesis, Stanford University, http://sepwww.stanford.edu/public/docs/sep91/.

Mulder, W. and R.-E. Plessix, 2004, Frequency-domain finite-frequency amplitude-preserving migration: Geophysical Journal International, **157**, 975–985.

Nemeth, T., C. Wu, and G. T. Schuster, 1999, Least-squares migration of incomplete reflection data: Geophysics, **64**, 208–221.

Rickett, J., 2003, Illumination-based normalization for wave-equation depth migration: Geophysics, **68**, 1371–1379.

Rickett, J. and D. E. Lumley, 2001, Cross-equalization data processing for time-lapse seismic reservoir monitoring: A case study from the Gulf of Mexico: Geophysics, **66**, 1015–1025.

Sarkar, S., W. P. Gouveia, and D. H. Johnston, 2003, On the inversion of time-lapse seismic data: SEG Technical Program Expanded Abstracts, **22**, 1489–1492.

Schmitt, U. and A. K. Louis, 2002, Efficient algorithms for the regularization of dynamic inverse problems: I. theory: Inverse Problems, **18**, 645–658.

Schmitt, U., A. K. Louis, C. Wolters, and M. Vauhkonen, 2002, Efficient algorithms for the regularization of dynamic inverse problems: Ii. applications: Inverse Problems, **18**, 659–676.

Shin, C., S. Jang, and D.-J. Min, 2001, Improved amplitude preservation for prestack depth migration by inverse scattering theory: Geophysical Prospecting, **49**, 592–606.

Symes, W. W., 2008, Approximate linearized inversion by optimal scaling of prestack depth migration: Geophysics, **73**, R23–R35.

Tang, Y., 2008a, Modeling, migration and inversion in the generalized source and receiver domain: SEP 136.

———, 2008b, Wave-equation hessian by phase encoding: SEP 134.

Valenciano, A., 2008, Imaging by Wave-Equation Inversion: PhD thesis, Stanford University.

Whitcombe, D. N., J. M. Marsh, P. J. Clifford, M. Dyce, C. J. S. McKenzie, S. Campbell, A. J. Hill, R. S. Parr, C. Pearse, T. A. Ricketts, C. P. Slater, and O. L. Barkved, 2004, The systematic application of 4D in BP's North-West Europe operations — 5 years on: SEG Technical Program Expanded Abstracts, **23**, 2251–2254.

Zhang, Y., A. Ghodrati, and D. H. Brooks, 2005, An analytical comparison of three spatio-temporal regularization methods for dynamic linear inverse problems in a common statistical framework: Inverse Problems, **21**, 357–382.

Zou, Y., L. R. Bentley, L. R. Lines, and D. Coombe, 2006, Integration of seismic methods with reservoir simulation, Pikes Peak heavy-oil field, Saskatchewan: The Leading Edge, **25**, 764–781.

APPENDIX A

JOINT-INVERSION FORMULATIONS FOR MULTIPLE SURVEYS

Here, we show a brief derivation of the joint-inversion formulation for two surveys and its generalization to multiple surveys.

Regularized joint-inversion

The process of acquiring two seismic datasets over an evolving earth model can be represented as

$$\begin{bmatrix} \mathbf{L}_0 & \mathbf{0} \\ \mathbf{0} & \mathbf{L}_1 \end{bmatrix} \begin{bmatrix} \mathbf{m}_0 \\ \mathbf{m}_1 \end{bmatrix} = \begin{bmatrix} \mathbf{d}_0 \\ \mathbf{d}_1 \end{bmatrix}, \tag{A-1}$$

where $\mathbf{d}_0$ and $\mathbf{d}_1$ are the baseline and monitor datasets, and $\mathbf{m}_0$ and $\mathbf{m}_1$ are the baseline and monitor reflectivity models respectively. The linear operators ($\mathbf{L}_0$ and $\mathbf{L}_1$) define the modeling/acquisition experiments for datasets $\mathbf{d}_0$ and $\mathbf{d}_1$ respectively. We rewrite equation A-1 to include spatial and regularization operators ($\mathbf{R}_0$ and $\mathbf{\Lambda}_0$ respectively), and we seek to minimize the objective function

$$S(\mathbf{m_0}, \mathbf{m_1}) = \left\| \left[\begin{array}{cc} \mathbf{L}_0 & \mathbf{0} \\ \mathbf{0} & \mathbf{L}_1 \\ \hline \mathbf{R}_0 & \mathbf{0} \\ \mathbf{0} & \mathbf{R}_1 \\ \hline -\mathbf{\Lambda}_0 & \mathbf{\Lambda}_1 \end{array} \right] \begin{bmatrix} \mathbf{m}_0 \\ \mathbf{m}_1 \end{bmatrix} - \begin{bmatrix} \mathbf{d}_0 \\ \mathbf{d}_1 \\ \mathbf{0} \\ \mathbf{0} \\ \mathbf{0} \end{bmatrix} \right\|^2. \tag{A-2}$$

This cost function can be expanded as follows:

$$\left(\begin{bmatrix} \mathbf{L'_0 L_0} & \mathbf{0} \\ \mathbf{0} & \mathbf{L'_1 L_1} \end{bmatrix} + \begin{bmatrix} \mathbf{R'_0 R_0} & \mathbf{0} \\ \mathbf{0} & \mathbf{R'_1 R_1} \end{bmatrix} + \begin{bmatrix} \mathbf{\Lambda'_0 \Lambda_0} & \mathbf{-\Lambda'_0 \Lambda_1} \\ \mathbf{-\Lambda'_1 \Lambda_0} & \mathbf{\Lambda'_1 \Lambda_1} \end{bmatrix} \right) \begin{bmatrix} \hat{\mathbf{m}}_0 \\ \hat{\mathbf{m}}_1 \end{bmatrix} = \begin{bmatrix} \tilde{\mathbf{m}}_0 \\ \tilde{\mathbf{m}}_1 \end{bmatrix}, \tag{A-3}$$

which can be written as

$$\left(\begin{bmatrix} \mathbf{H_0} & \mathbf{0} \\ \mathbf{0} & \mathbf{H_1} \end{bmatrix} + \begin{bmatrix} \mathbf{R_{00}} & \mathbf{0} \\ \mathbf{0} & \mathbf{R_{11}} \end{bmatrix} + \begin{bmatrix} \mathbf{\Lambda_{00}} & \mathbf{-\Lambda_{01}} \\ \mathbf{-\Lambda_{10}} & \mathbf{\Lambda_{11}} \end{bmatrix} \right) \begin{bmatrix} \hat{\mathbf{m}}_0 \\ \hat{\mathbf{m}}_1 \end{bmatrix} = \begin{bmatrix} \tilde{\mathbf{m}}_0 \\ \tilde{\mathbf{m}}_1 \end{bmatrix}, \tag{A-4}$$

where

$$\begin{aligned} \mathbf{R_{ij}} &= \mathbf{\epsilon_i R'_i \epsilon_j R_j}, \\ \mathbf{\Lambda_{ij}} &= \mathbf{\zeta_i \Lambda'_i \zeta_j \Lambda_j}, \end{aligned} \tag{A-5}$$

while $\mathbf{R_0}$ and $\mathbf{R_1}$ are the spatial/imaging constraints for the baseline and monitor images respectively, and $\mathbf{\Lambda_0}$ and $\mathbf{\Lambda_1}$ the temporal constraints between the surveys. The parameters $\epsilon_\mathbf{0}$ and $\epsilon_\mathbf{1}$ determine the strength of the spatial regularization on the baseline and monitor images respectively, while $\zeta_\mathbf{0}$ and $\zeta_\mathbf{1}$ determine the coupling between surveys. Equation A-4 is the RJMI formulation. Using a similar procedure, the RJID formulation for two seismic datasets can be shown to be

$$\left(\begin{bmatrix} \mathbf{H_0}+\mathbf{H_1} & \mathbf{H_1} \\ \mathbf{H_1} & \mathbf{H_1} \end{bmatrix} + \begin{bmatrix} \mathbf{R_{00}} & \mathbf{0} \\ \mathbf{0} & \mathbf{R_{11}} \end{bmatrix} + \begin{bmatrix} \mathbf{\Lambda_{00}} & \mathbf{0} \\ -\mathbf{\Lambda_{10}} & \mathbf{\Lambda_{11}} \end{bmatrix}\right) \begin{bmatrix} \hat{\mathbf{m}}_0 \\ \Delta\hat{\mathbf{m}}_1 \end{bmatrix} = \begin{bmatrix} \tilde{\mathbf{m}}_0+\tilde{\mathbf{m}}_1 \\ \tilde{\mathbf{m}}_1 \end{bmatrix}. \tag{A-6}$$

In the next sections, we derive the RJID and RJMI formulations for multiple surveys.

Regularized joint-inversion of multiple images: RJMI

The data modeling process for three seismic datasets (a baseline and two monitors) over an evolving earth model can be written as

$$\begin{bmatrix} \mathbf{L}_0 & \mathbf{0} & \mathbf{0} \\ \mathbf{0} & \mathbf{L}_1 & \mathbf{0} \\ \mathbf{0} & \mathbf{0} & \mathbf{L}_2 \end{bmatrix} \begin{bmatrix} \mathbf{m}_0 \\ \mathbf{m}_1 \\ \mathbf{m}_2 \end{bmatrix} = \begin{bmatrix} \mathbf{d}_0 \\ \mathbf{d}_1 \\ \mathbf{d}_2 \end{bmatrix}, \tag{A-7}$$

where $\mathbf{d}_0$, $\mathbf{d}_1$ and $\mathbf{d}_2$ are respectively datasets for the baseline, first and second monitor, $\mathbf{m}_0$, $\mathbf{m}_1$, and $\mathbf{m}_2$ are the baseline and monitor reflectivity models. The linear operators ($\mathbf{L}_0$, $\mathbf{L}_1$ and $\mathbf{L}_2$) define the modeling/acquisition experiments for datasets $\mathbf{d}_0$, $\mathbf{d}_1$ and $\mathbf{d}_2$ respectively. The least-squares solution to equation A-7 is given as

$$\begin{bmatrix} \mathbf{L'_0L_0} & \mathbf{0} & \mathbf{0} \\ \mathbf{0} & \mathbf{L'_1L_1} & \mathbf{0} \\ \mathbf{0} & 0 & \mathbf{L'_2L_2} \end{bmatrix} \begin{bmatrix} \hat{\mathbf{m}}_0 \\ \hat{\mathbf{m}}_1 \\ \hat{\mathbf{m}}_2 \end{bmatrix} = \begin{bmatrix} \mathbf{L'}_0 & \mathbf{0} & \mathbf{0} \\ \mathbf{0} & \mathbf{L'}_1 & \mathbf{0} \\ \mathbf{0} & \mathbf{0} & \mathbf{L'}_2 \end{bmatrix} \begin{bmatrix} \mathbf{d}_0 \\ \mathbf{d}_1 \\ \mathbf{d}_2 \end{bmatrix}, \tag{A-8}$$

where the symbol $'$ denotes transposed complex conjugate.

We rewrite equation A-8 as

$$\begin{bmatrix} \mathbf{H_0} & \mathbf{0} & \mathbf{0} \\ \mathbf{0} & \mathbf{H_1} & \mathbf{0} \\ \mathbf{0} & \mathbf{0} & \mathbf{H_2} \end{bmatrix} \begin{bmatrix} \hat{\mathbf{m}}_0 \\ \hat{\mathbf{m}}_1 \\ \hat{\mathbf{m}}_2 \end{bmatrix} = \begin{bmatrix} \tilde{\mathbf{m_0}} \\ \tilde{\mathbf{m_1}} \\ \tilde{\mathbf{m_2}} \end{bmatrix}, \tag{A-9}$$

where $\tilde{\mathbf{m}}_\mathbf{i}$ is the migrated image from the $\mathbf{i}^{th}$ survey, and $\mathbf{H_i}$ is the corresponding Hessian matrix. Introducing spatial and temporal constraints into equation A-9 we obtain

$$\left(\begin{bmatrix} \mathbf{H_0} & \mathbf{0} & \mathbf{0} \\ \mathbf{0} & \mathbf{H_1} & \mathbf{0} \\ \mathbf{0} & \mathbf{0} & \mathbf{H_2} \end{bmatrix} + \begin{bmatrix} \mathbf{R_{00}} & \mathbf{0} & \mathbf{0} \\ \mathbf{0} & \mathbf{R_{11}} & \mathbf{0} \\ \mathbf{0} & \mathbf{0} & \mathbf{R_{22}} \end{bmatrix} + \begin{bmatrix} \mathbf{\Lambda_{00}} & -\mathbf{\Lambda_{01}} & \mathbf{0} \\ -\mathbf{\Lambda_{10}} & \mathbf{2\Lambda_{11}} & -\mathbf{\Lambda_{12}} \\ \mathbf{0} & -\mathbf{\Lambda_{21}} & \mathbf{\Lambda_{22}} \end{bmatrix}\right) \begin{bmatrix} \hat{\mathbf{m}}_0 \\ \hat{\mathbf{m}}_1 \\ \hat{\mathbf{m}}_2 \end{bmatrix} = \begin{bmatrix} \tilde{\mathbf{m_0}} \\ \tilde{\mathbf{m_1}} \\ \tilde{\mathbf{m_2}} \end{bmatrix}. \tag{A-10}$$

Equation A-10 can be generalized to an arbitrary number of surveys as follows

$$[\boldsymbol{\Xi} + \Re + \boldsymbol{\Gamma}] \left[\hat{\mathbf{M}}\right] = \left[\tilde{\mathbf{M}}\right], \tag{A-11}$$

where, $\boldsymbol{\Xi}$ is the Hessian operator, defined as

$$\boldsymbol{\Xi} = \begin{bmatrix} \mathbf{H_0} & \mathbf{0} & \mathbf{0} & ... & \mathbf{0} & \mathbf{0} \\ \mathbf{0} & \mathbf{H_1} & \mathbf{0} & ... & \mathbf{0} & \mathbf{0} \\ \mathbf{0} & \mathbf{0} & \mathbf{H_2} & ... & ... & \mathbf{0} \\ : & : & : & : & : & : \\ : & : & : & : & \mathbf{H_{N-1}} & \mathbf{0} \\ \mathbf{0} & \mathbf{0} & \mathbf{0} & ... & \mathbf{0} & \mathbf{H_N} \end{bmatrix}. \tag{A-12}$$

The spatial and temporal regularization operators, $\Re$ and $\boldsymbol{\Gamma}$ are defined as

$$\begin{aligned} \Re &= \mathbf{R}'\mathbf{R}, \\ \boldsymbol{\Gamma} &= \boldsymbol{\Lambda}'\boldsymbol{\Lambda}, \end{aligned} \tag{A-13}$$

where,

$$\mathbf{R} = \begin{bmatrix} \mathbf{R_0} & \mathbf{0} & \mathbf{0} & ... & \mathbf{0} & \mathbf{0} \\ \mathbf{0} & \mathbf{R_1} & \mathbf{0} & ... & \mathbf{0} & \mathbf{0} \\ \mathbf{0} & \mathbf{0} & \mathbf{R_2} & ... & \mathbf{0} & \mathbf{0} \\ : & : & : & : & : & : \\ : & : & : & \mathbf{0} & \mathbf{R_{N-1}} & \mathbf{0} \\ \mathbf{0} & \mathbf{0} & \mathbf{0} & \mathbf{0} & \mathbf{0} & \mathbf{R_N} \end{bmatrix}, \tag{A-14}$$

and,

$$\boldsymbol{\Lambda} = \begin{bmatrix} \mathbf{\Lambda_0} & \mathbf{\Lambda_1} & \mathbf{0} & \mathbf{0} & ... & \mathbf{0} \\ \mathbf{0} & -\mathbf{\Lambda_1} & \mathbf{\Lambda_2} & \mathbf{0} & ... & \mathbf{0} \\ \mathbf{0} & \mathbf{0} & -\mathbf{\Lambda_2} & -\mathbf{\Lambda_3} & ... & \mathbf{0} \\ : & : & : & : & : & : \\ \mathbf{0} & \mathbf{0} & ... & \mathbf{0} & -\mathbf{\Lambda_{N-1}} & \mathbf{\Lambda_N} \\ \mathbf{0} & \mathbf{0} & ... & \mathbf{0} & \mathbf{0} & \mathbf{\Lambda_N} \end{bmatrix}. \tag{A-15}$$

The input vector into the RJMI formulation, $\tilde{\mathbf{M}}$ is given as

$$\tilde{\mathbf{M}} = \begin{bmatrix} \tilde{\mathbf{m}}_0 \\ \tilde{\mathbf{m}}_1 \\ \tilde{\mathbf{m}}_2 \\ : \\ \tilde{\mathbf{m}}_{N-1} \\ \tilde{\mathbf{m}}_N \end{bmatrix}, \tag{A-16}$$

while the inversion targets are in the vector:

$$\hat{\mathbf{M}} = \begin{bmatrix} \hat{\mathbf{m}}_0 \\ \hat{\mathbf{m}}_1 \\ \hat{\mathbf{m}}_2 \\ : \\ \hat{\mathbf{m}}_{N-1} \\ \hat{\mathbf{m}}_N \end{bmatrix}. \tag{A-17}$$

Regularized joint-inversion for image differences: RJID

The data modeling process for three seismic datasets over an evolving earth model can be written as

$$\begin{bmatrix} \mathbf{L}_0 & \mathbf{0} & \mathbf{0} \\ \mathbf{L}_1 & \mathbf{L}_1 & \mathbf{0} \\ \mathbf{L}_2 & \mathbf{L}_2 & \mathbf{L}_2 \end{bmatrix} \begin{bmatrix} \mathbf{m}_0 \\ \Delta\mathbf{m}_1 \\ \Delta\mathbf{m}_2 \end{bmatrix} = \begin{bmatrix} \mathbf{d}_0 \\ \mathbf{d}_1 \\ \mathbf{d}_2 \end{bmatrix}, \tag{A-18}$$

where $\mathbf{d}_0$, $\mathbf{d}_1$ and $\mathbf{d}_2$ are respectively datasets for the baseline, first and second monitor, $\mathbf{m}_0$ is the baseline reflectivity and the time-lapse reflectivities $\Delta\mathbf{m}_1$ and $\Delta\mathbf{m}_2$ are defined as

$$\begin{aligned} \Delta\mathbf{m}_1 &= \mathbf{m}_1 - \mathbf{m}_0, \\ \Delta\mathbf{m}_2 &= \mathbf{m}_2 - \mathbf{m}_1, \end{aligned} \tag{A-19}$$

where $\mathbf{m}_1$ and $\mathbf{m}_2$ are respectively the monitor reflectivities at the times data $\mathbf{d}_1$ and $\mathbf{d}_2$ were acquired (with survey geometries defined by the linear $\mathbf{L}_1$ and $\mathbf{L}_2$).

The least-squares solution to equation A-18 is given as

$$\begin{bmatrix} \mathbf{L'_0L_0} + \mathbf{L'_1L_1} + \mathbf{L'_2L_2} & \mathbf{L'_1L_1} + \mathbf{L'_2L_2} & \mathbf{L'_2L_2} \\ \mathbf{L'_1L_1} + \mathbf{L'_2L_2} & \mathbf{L'_1L_1} + \mathbf{L'_2L_2} & \mathbf{L'_2L_2} \\ \mathbf{L'_2L_2} & \mathbf{L'_2L_2} & \mathbf{L'_2L_2} \end{bmatrix} \begin{bmatrix} \hat{\mathbf{m}}_0 \\ \Delta\hat{\mathbf{m}}_1 \\ \Delta\hat{\mathbf{m}}_2 \end{bmatrix} = \begin{bmatrix} \mathbf{L'}_0 & \mathbf{L'}_1 & \mathbf{L'}_2 \\ & \mathbf{L'}_1 & \mathbf{L'}_2 \\ & & \mathbf{L'}_2 \end{bmatrix} \begin{bmatrix} \mathbf{d}_0 \\ \mathbf{d}_1 \\ \mathbf{d}_2 \end{bmatrix}, \tag{A-20}$$

where the symbol $'$ denotes transpose complex conjugate. We rewrite equation A-20 as

$$\begin{bmatrix} \mathbf{H_0} + \mathbf{H_1} + \mathbf{H_2} & \mathbf{H_1} + \mathbf{H_2} & \mathbf{H_2} \\ \mathbf{H_1} + \mathbf{H_2} & \mathbf{H_1} + \mathbf{H_2} & \mathbf{H_2} \\ \mathbf{H_2} & \mathbf{H_2} & \mathbf{H_2} \end{bmatrix} \begin{bmatrix} \hat{\mathbf{m}}_0 \\ \Delta\hat{\mathbf{m}}_1 \\ \Delta\hat{\mathbf{m}}_2 \end{bmatrix} = \begin{bmatrix} \tilde{\mathbf{m_0}} + \tilde{\mathbf{m_1}} + \tilde{\mathbf{m_2}} \\ \tilde{\mathbf{m_1}} + \tilde{\mathbf{m_2}} \\ \tilde{\mathbf{m_2}} \end{bmatrix}, \tag{A-21}$$

where $\tilde{\mathbf{m_i}}$ is the migrated image from the $\mathbf{i}^{th}$ survey, and $\mathbf{H_i}$ is the corresponding Hessian matrix. Introducing spatial and temporal regularization goals that incorporates prior knowledge of the reservoir geometry and location as well as constraints on the inverted time-lapse images into equation A-21 we obtain

$$\begin{aligned} \left(\begin{bmatrix} \mathbf{H_0} + \mathbf{H_1} + \mathbf{H_2} & \mathbf{H_1} + \mathbf{H_2} & \mathbf{H_2} \\ \mathbf{H_1} + \mathbf{H_2} & \mathbf{H_1} + \mathbf{H_2} & \mathbf{H_2} \\ \mathbf{H_2} & \mathbf{H_2} & \mathbf{H_2} \end{bmatrix} + \begin{bmatrix} \mathbf{R_{00}} & \mathbf{0} & \mathbf{0} \\ \mathbf{0} & \mathbf{R_{11}} & \mathbf{0} \\ \mathbf{0} & \mathbf{0} & \mathbf{R_{22}} \end{bmatrix} \right. \\ \left. + \begin{bmatrix} \mathbf{\Lambda_{00}} & \mathbf{0} & \mathbf{0} \\ \mathbf{0} & \mathbf{2\Lambda_{11}} & \mathbf{-\Lambda_{12}} \\ \mathbf{0} & \mathbf{-\Lambda_{21}} & \mathbf{\Lambda_{22}} \end{bmatrix} \right) \begin{bmatrix} \hat{\mathbf{m}}_0 \\ \Delta\hat{\mathbf{m}}_1 \\ \Delta\hat{\mathbf{m}}_2 \end{bmatrix} = \begin{bmatrix} \tilde{\mathbf{m_0}} + \tilde{\mathbf{m_1}} + \tilde{\mathbf{m_2}} \\ \tilde{\mathbf{m_1}} + \tilde{\mathbf{m_2}} \\ \tilde{\mathbf{m_2}} \end{bmatrix}, \end{aligned} \tag{A-22}$$

where,

$$\begin{aligned} \mathbf{R_{ij}} &= \epsilon_\mathbf{i}\mathbf{R'}_\mathbf{i}\epsilon_\mathbf{j}\mathbf{R_j} \\ \mathbf{\Lambda_{ij}} &= \zeta_\mathbf{i}\mathbf{\Lambda'}_\mathbf{i}\zeta_\mathbf{j}\mathbf{\Lambda_j} \end{aligned}, \tag{A-23}$$

with $\mathbf{R_i}$ being the spatial regularization terms for the baseline and time-lapse images respectively while $\mathbf{\Lambda_i}$ is the temporal regularization between the surveys. Note that

$\mathbf{R_{ij}}$ and $\mathbf{\Lambda_{ij}}$ are not explicitly computed, but instead, the regularization operators $\mathbf{R_i}$ and $\mathbf{\Lambda_i}$ (and their adjoints) are applied at each step of the inversion. Parameters ϵ_i and ζ_i determine the relative strengths of the spatial and temporal regularization respectively. Equation A-22 can be generalized to an arbitrary number of surveys as follows

$$[\mathbf{\Xi} + \Re + \mathbf{\Gamma}] \left[\hat{\mathbf{M}}\right] = \left[\tilde{\mathbf{M}}\right], \tag{A-24}$$

where, $\mathbf{\Xi}$ is the Hessian operator, defined as

$$\mathbf{\Xi} = \begin{bmatrix} \mathbf{H_0} + .. + \mathbf{H_N} & \mathbf{H_1} + .. + \mathbf{H_N} & \mathbf{H_2} + .. + \mathbf{H_N} & ... & \mathbf{H_{N-1}} + \mathbf{H_N} & \mathbf{H_N} \\ \mathbf{H_1} + .. + \mathbf{H_N} & \mathbf{H_1} + .. + \mathbf{H_N} & \mathbf{H_2} + .. + \mathbf{H_N} & ... & \mathbf{H_{N-1}} + \mathbf{H_N} & \mathbf{H_N} \\ \mathbf{H_2} + .. + \mathbf{H_N} & \mathbf{H_2} + .. + \mathbf{H_N} & \mathbf{H_2} + .. + \mathbf{H_N} & ... & ... & \mathbf{H_N} \\ : & : & : & : & : & : \\ : & : & : & : & \mathbf{H_{N-1}} + \mathbf{H_N} & \mathbf{H_N} \\ \mathbf{H_N} & \mathbf{H_N} & \mathbf{H_N} & ... & \mathbf{N_N} & \mathbf{H_N} \end{bmatrix}. \tag{A-25}$$

The regularization operators $\Re$ and $\mathbf{\Gamma}$ are defined as

$$\begin{aligned} \Re &= \mathbf{R}'\mathbf{R}, \\ \mathbf{\Gamma} &= \mathbf{\Lambda}'\mathbf{\Lambda}, \end{aligned} \tag{A-26}$$

where,

$$\mathbf{R} = \begin{bmatrix} \mathbf{R_0} & \mathbf{0} & \mathbf{0} & ... & \mathbf{0} & \mathbf{0} \\ \mathbf{0} & \mathbf{R_1} & \mathbf{0} & ... & \mathbf{0} & \mathbf{0} \\ \mathbf{0} & \mathbf{0} & \mathbf{R_2} & ... & \mathbf{0} & \mathbf{0} \\ : & : & : & : & : & : \\ : & : & : & \mathbf{0} & \mathbf{R_{N-1}} & \mathbf{0} \\ \mathbf{0} & \mathbf{0} & \mathbf{0} & \mathbf{0} & \mathbf{0} & \mathbf{R_N} \end{bmatrix}, \tag{A-27}$$

and,

$$\mathbf{\Lambda} = \begin{bmatrix} \mathbf{\Lambda_0} & \mathbf{0} & \mathbf{0} & \mathbf{0} & ... & \mathbf{0} \\ \mathbf{0} & -\mathbf{\Lambda_1} & \mathbf{\Lambda_2} & \mathbf{0} & ... & \mathbf{0} \\ \mathbf{0} & \mathbf{0} & -\mathbf{\Lambda_2} & -\mathbf{\Lambda_3} & ... & \mathbf{0} \\ : & : & : & : & : & : \\ \mathbf{0} & \mathbf{0} & ... & \mathbf{0} & -\mathbf{\Lambda_{N-1}} & \mathbf{\Lambda_N} \\ \mathbf{0} & \mathbf{0} & ... & \mathbf{0} & \mathbf{0} & \mathbf{\Lambda_N} \end{bmatrix}. \tag{A-28}$$

The input vector into the RJID formulation, $\tilde{\mathbf{M}}$ is given as

$$\tilde{\mathbf{M}} = \begin{bmatrix} \tilde{\mathbf{m_0}} + ... + \tilde{\mathbf{m}}_N \\ \tilde{\mathbf{m_1}} + ... + \tilde{\mathbf{m}}_N \\ \tilde{\mathbf{m_2}} + ... + \tilde{\mathbf{m}}_N \\ : \\ \tilde{\mathbf{m}}_{N-1} + \tilde{\mathbf{m}}_N \\ \tilde{\mathbf{m}}_N \end{bmatrix}, \tag{A-29}$$

while the inversion targets are

$$\hat{\mathbf{M}} = \begin{bmatrix} \hat{\mathbf{m}}_0 \\ \Delta\hat{\mathbf{m}}_1 \\ \Delta\hat{\mathbf{m}}_2 \\ \vdots \\ \vdots \\ \Delta\hat{\mathbf{m}}_N \end{bmatrix}. \tag{A-30}$$

The temporal constraint on the baseline image, $\mathbf{\Lambda_0}$ may be set to zero, since it is assumed that the original geological structure is unchanged over time or that geomechanical changes are accounted for before/during inversion.